



Ultrafast optical polarimetry in magnetic phases of the Kondo semimetal CeSb

M. Naseska ¹, N. D. Zhigadlo,² Z. Jagličič,^{3,4} E. Goreshnik,⁵ and T. Mertelj ^{1,6,*}

¹*Department of Complex Matter, Jozef Stefan Institute, Jamova 39, 1000 Ljubljana, Slovenia*

²*CrystMat Company, CH-8037 Zurich, Switzerland*

³*Faculty of Civil and Geodetic Engineering, University of Ljubljana, Jamova cesta 2, Ljubljana, Slovenia*

⁴*Institute of Mathematics, Physics and Mechanics, Jadranska 19, Ljubljana, Slovenia*

⁵*Department of Inorganic Chemistry and Technology, Jozef Stefan Institute, Jamova 39, 1000 Ljubljana, Slovenia*

⁶*Center of Excellence for Nanoscience and Nanotechnology (CENN Nanocenter), Jamova 39, 1000 Ljubljana, Slovenia*



(Received 5 September 2023; revised 5 January 2024; accepted 1 March 2024; published 21 March 2024)

We investigated photoinduced ultrafast transient dynamics in different magnetic phases in CeSb by means of time resolved magneto-optical spectroscopy. We observe distinctive coherent oscillations in the ground-state antiferromagnetic (AF) phase and the high-magnetic-field ferromagnetic (F) phase. While the AF-phase oscillation frequencies match the recent Raman scattering findings the F-phase oscillation frequency does not correspond to the previously observed magnetic excitation. The large spectroscopic factor, $g = 3.94$, and optical polarization properties suggest that it corresponds to a previously undetected Ce^{3+} coherent crystal-field state excitation. The AF-phase oscillations show no magnetic-field dependence so their lattice origin cannot be entirely excluded. The nonoscillatory part of the transients is qualitatively similar in all investigated magnetic phases with a faster subpicosecond dynamics in the ferromagnetic and ferroparamagnetic phases and is attributed to differences in the electronic structure, which affect the photoexcited quasiparticle energy relaxation kinetics.

DOI: [10.1103/PhysRevB.109.125140](https://doi.org/10.1103/PhysRevB.109.125140)

I. INTRODUCTION

CeSb is a material that has one of the most complex phase diagrams among lanthanide monopnictides. It contains at least 16 different magnetic phases in the H - T plane [1] comprising different sequences of ferromagnetic (F), with either up or down spin orientation, and paramagnetic (P) (001) planes stacked along the c axis [1,2]. The complexity is thought to arise from the interplay of Kondo, spin-orbit, and crystal-field effects as well as the Sb- $5p$ and Ce- $4d$ orbital mixing [3–5]. Lattice modulation in the magnetic phases was also observed [6].

The phase diagram [1,2] (see Fig. 1) and some magnetic excitations [3,7] were thoroughly studied by neutron scattering. Recently the sensitivity of the electronic structure to the magnetic phase has been demonstrated [8] and additional magnetic excitations were found in the ground-state AF phase [9]. While the main features of the magnetic behavior are understood and successfully modeled using an effective interaction approach [5] the microscopic origin of the interactions is still puzzling [4,9]. An insight into nonequilibrium dynamics of different phases might therefore shed some light on the interplay between different degrees of freedom.

Here we present and discuss our investigation of the ultrafast nonequilibrium dynamics upon photoexcitation in different magnetic phases in CeSb with a focus on the magnetic excitations in the weakly nonequilibrium photoexcited state. We confirm the presence of the recently reported [9]

additional modes in the ground-state AF phase and show that their frequencies are magnetic-field independent. In the high-magnetic-field F phase we identify a previously unobserved ${}^2E_{2g}$ Ce^{3+} crystal-field excited state. The associated coherent oscillatory optical response can be linked to the *real-time quantum evolution* of the superposition state involving the ground state and a particular excited crystal-field state.

II. EXPERIMENTAL

A. Samples

CeSb is the only congruently melting compound in the Ce-Sb phase diagram with a relatively high melting temperature ($T_m = 1760$ °C), and its crystals can be grown by simply cooling a stoichiometric mixture of Ce and Sb, or out of a Sn-rich flux [11]. The present samples were produced by two-step process. High-purity Ce (4N) and Sb (4N) were prereacted at 650 °C in evacuated quartz ampule in the first step. The resultant powder was then compressed into a pellet and put inside a molybdenum crucible. The sealed crucible was heated to a temperature above the melting point of CeSb, then slowly cooled to a temperature about 40 °C below the melting temperature, maintained there for about a week, and finally cooled to room temperature. Nicely formed single crystals up to $3 \times 3 \times 3$ mm³ in volume were collected. The 1 : 1 stoichiometry and excellent structural quality of the produced crystals were confirmed by energy dispersive x-ray spectroscopy and x-ray diffraction studies.

The single crystal used for the optical measurements was also characterized by superconducting quantum interference

*tomaz.mertelj@ijs.si

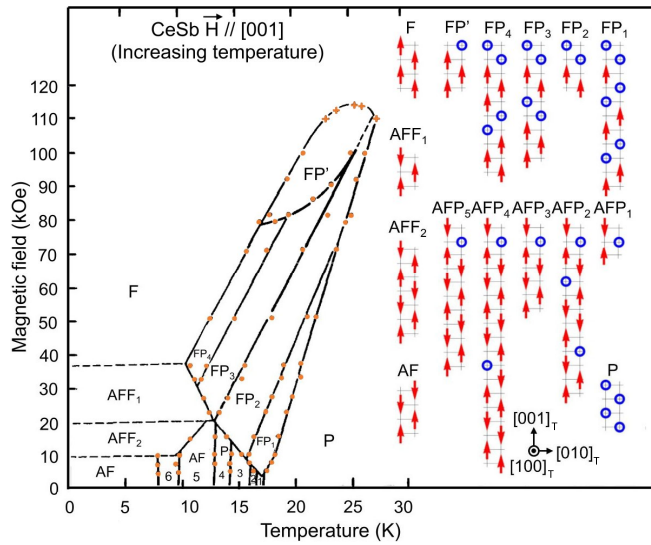


FIG. 1. Magnetic phase diagram of CeSb adapted from Rossat-Mignod *et al.* [2] and Ye *et al.* [10]. Each red arrow represents a single ferromagnetically ordered (001) plane while the blue circles represent the paramagnetic (001) planes. The neighboring planes are due to the face centered cubic structure shifted relatively by $[0\frac{1}{2}\frac{1}{2}]$ (or $[\frac{1}{2}0\frac{1}{2}]$).

device magnetometry. The low-field T scan and low- T field magnetization scans shown in Figs. 2(b) and 2(d) were found consistent with the published phase diagram [2,12] (Fig. 1).

B. Optical measurements

The sample was mounted in a 7-T optical split-coil cryomagnet with transverse optical access. The pump (3.1-eV photon energy) and probe (1.55-eV photon energy) pulse-train beams (pulse length <100 fs, 250-kHz repetition rate) were focused in a nearly perpendicular manner on a [001] cleaved crystal facet [see Fig. 2(c)]. The magnetic field was lying

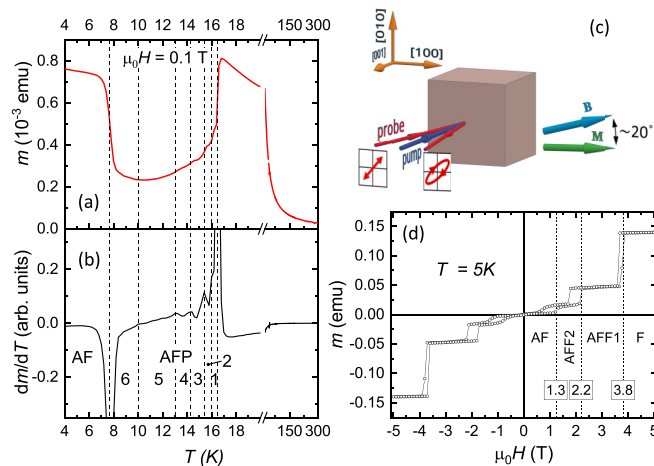


FIG. 2. Sample characterization data and the optical setup geometry. (a) The low-field magnetic moment of the sample as a function of T . (b) The corresponding derivative. (c) The time resolved polarimetry setup geometry. (d) The low- T magnetic moment as a function of magnetic field.

in the facet plane at $\approx 20^\circ$ with respect to the [100] cubic direction, while the probe polarization was oriented approximately along the [110] direction (unless specified differently) to maximize the transient polarization rotation.

The beam diameters of slightly elliptical beams were of similar size. The probe beam diameter was $(64 \times 52) \mu\text{m}^2$ and the pump beam diameter was $(80 \times 76) \mu\text{m}^2$. The fluence of the probe in all measurements was around $4 \mu\text{J}/\text{cm}^2$ and the pump beam fluence was in the interval between 60 and $90 \mu\text{J}/\text{cm}^2$ (unless specified differently).

The reflected probe beam transient polarization rotation, $\Delta\Phi$, was acquired using a Wollaston prism and a pair of balanced silicon PIN photodiodes using the standard lock-in techniques. The scattered pump contribution was suppressed by means of a long-pass optical filter. The detector was kept carefully balanced to avoid contamination of the $\Delta\Phi$ signal with the isotropic part of the transient reflectivity, $\Delta R/R$, response. To measure $\Delta R/R$ the detector was rotated to maximize the DC current component on one of the PIN diodes while the other PIN diode was disconnected.

Since zero field cooling resulted in multidomain states and nonreproducible transients the sample was always field cooled at $\mu_0 H = 7$ T in order to achieve a monodomain magnetic state [1]. Due to the field cooling the $[001]_T$ tetragonal direction and the spin orientations are along the $[100]$ pseudocubic direction [1] in the F, FP_n , and AFF_n phases (see Fig. 1 for designation of the phases). In the ground-state AF phase we observed an angular momentum flop (discussed later) resulting in the $[001]_T$ direction and spin direction rotation to the $[010]$ pseudocubic direction. In the rest of the paper we use the pseudocubic notation tacitly assuming the above orientations.

III. RESULTS

A. Overview of the phases

In order to more clearly present our data we start with a brief overview of the magnetic structures shown in Fig. 1. In the absence of an external magnetic field the low- T magnetic AF ground state corresponds to a four-sublattice collinear antiferromagnet where ferromagnetically ordered plane pairs align antiferromagnetically, $\uparrow\uparrow\downarrow\downarrow$. With increasing T a series of six, more complicated, antiferromagnetic phases (AFP_n) are found, where one or more, $\uparrow\circ\downarrow$ or $\downarrow\circ\uparrow$, 3-tuples, containing a paramagnetic plane (\circ) in the middle, are inserted between the ferromagnetic pairs. This leads to long period (up to 13 planes) magnetic unit cells. Application of an external field leads to a F phase through a sequence of metamagnetic transitions. Below $T \approx 12$ K the metamagnetic transitions lead to two ferrimagnetic phases. The higher-field one, AFF_1 , is composed from the $\uparrow\uparrow\downarrow$ 3-tuples, while the lower-field one corresponds to the sequence of the AF unit cells interleaved with the $\uparrow\uparrow\downarrow$ 3-tuples. Above $T \approx 10$ K five additional ferromagnetic phases (FP_n and FP') that contain paramagnetic planes inserted between the ferromagnetic planes appear. In the FP_n phases the paramagnetic planes form pairs, $\circ\circ$.

B. Transient data overview

In Fig. 3 we show selected polarization rotation transients. A typical transient displays a fast subpicosecond rise followed

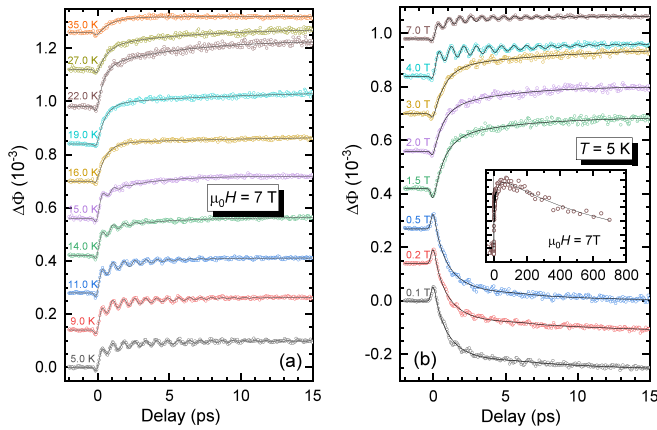


FIG. 3. (a) Transient polarization rotation at selected T at $\mu_0H = 7$ T (measured on warming) and (b) at selected μ_0H at $T = 5$ K (measured on decreasing field). The traces are vertically shifted for clarity. A typical longer timescale evolution of the signal is shown in the inset to (b). The lines correspond to the fits discussed in text.

by a slower increase on tens-of-picoseconds timescale and a nanosecond recovery. In the F and AF phases coherent oscillations are present within the first ≈ 10 ps. At all fields and temperatures we observe also an initial relatively small fast transient (≈ 200 fs) with the opposite sign to the dominant transient. The transient reflectivity [see Fig. 11(b)] shows a similar shape, but was not studied in detail.

The transients show no pump-polarization dependence while the probe polarization dependence is strong and consistent with the low- T tetragonal symmetry (see also Appendix C) with the c axis and the (sublattice) magnetization along either the [100] or [010] direction. As shown in Fig. 4 $\Delta R/R$ shows extrema along the [100] and [010] directions while $\Delta\Phi$ is shifted by $\approx 45^\circ$ with extrema close to the [110] direction.

The coherent oscillations are clear and strong in the F phase [see the low- T high-field scans in Fig. 3(a)]. With decreasing magnetic field [Fig. 3(b)] below $\mu_0H \approx 4$ T, in the AFF_1 phase, the coherent oscillations vanish and the subpicosecond rise time increases. Decreasing the field further leads to

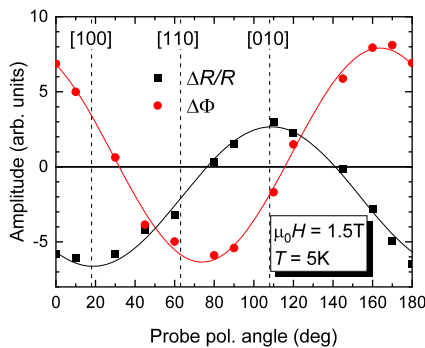


FIG. 4. Angular dependence of the transient reflectivity and polarization rotation amplitudes (see also Fig. 11) in the AFF_2 phase. The full lines are harmonic fits. The angle is measured relative to the direction of the magnetic field. The vertical dashed lines indicate the approximate orientation of the crystal directions.

another qualitative change of the response below $\mu_0H \approx 1$ T, in the AF phase, where the response changes sign and the coherent oscillations reappear, albeit weaker than in the F phase. The sign change in the AF phase is consistent with rotation of the tetragonal c axis and sublattice magnetizations around the surface normal ([001] pseudocubic direction) by 90° . In other phases no coherent oscillations could be clearly and reproducibly observed above the noise floor.¹

C. Analysis

In order to extract some quantitative information from the transient polarization rotation we use a phenomenological displacive excitation of a coherent oscillator (DECO) model [14] fit to the data in the F phase (see Appendix B for details), where the coherent oscillations are strong. In other phases, where the coherent oscillations are weaker or absent, a simpler three-exponential component model is used.

While one would expect that even in simpler ferromagnets, governed by the Landau-Lifshitz-Gilbert equation, the dynamics would be richer than that of a single scalar oscillator, the DECO model can describe the F-phase coherent oscillations surprisingly well. Due to the absence of any beating pattern a single displacive coherent oscillator is assumed. However, in order to fully describe the transients and the coherent-oscillations phase the displacement, A_{displ} , that drives the oscillator needs to be modeled by a sum of three pulse-driven exponential components with different relaxation times:

$$A_{\text{displ}}(t) = \sum_j A_{Oj} \int_0^\infty g(t-u) \exp^{-u/\tau_j} du. \quad (1)$$

Here $g(u)$ corresponds to a normalized Gaussian driving pulse shape, A_{Oj} corresponds to the amplitudes, and τ_j corresponds to the relaxation times. The two exponential components with the amplitudes A_{O1} and A_{O2} and relaxation times $\tau_1 \approx 0.3$ – 1 ps and $\tau_2 \approx 5$ – 20 ps, respectively, are used to model the rise time while the third, with a fixed (very slow) relaxation time, τ_∞ , and the amplitude $A_{O\infty}$, was used to fit the tens-of-picoseconds plateau (see Fig. 5). Since the data were acquired mostly only on short intervals up to 15 ps the actual values of τ_∞ cannot be obtained from the fits. A limited number of nanosecond-interval scans indicate that the actual value of τ_∞ is ≈ 0.8 ns [see inset to Fig. 3(b)]; however, detailed T and H dependencies were not determined, so a large unbiased value of $\tau_\infty = 10$ ns was assumed for the fits.

In general, each of the exponential displacement components can also contribute to the optical response directly in the same way as to $A_{\text{displ}}(t)$, but with independent amplitudes, A_{ej} [see Eq. (B1) for details]. In the F phase we were able to fit the data by setting $A_{e2} = A_{e\infty} = 0$, while a finite A_{e1} was necessary to completely fit the sub-200-fs dynamics. In other phases all three exponential amplitudes A_{e1} , A_{e2} , and $A_{e\infty}$, corresponding to τ_1 , τ_2 , and τ_∞ , respectively, were finite, while all A_{Oj} are set to zero. The selected fits in different phases are shown as lines in Fig. 3.

¹No data were acquired in the AFP_n phases, which remain to be the subject of further studies.

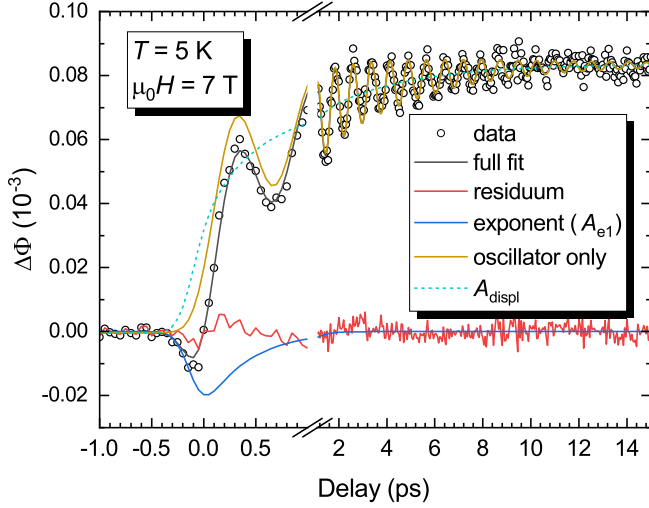


FIG. 5. DECO fit components in the F phase. The dashed line represents the instant oscillator equilibrium position.

Moreover, to obtain fair fits around the zero delay the effective pump-probe pulse cross-correlation width τ_p was used as a global free parameter across the given data set to take into account the initial fast processes that are not included in the model as a separate component. This reduced the number of fit parameters and improved the fit convergence with minimal deterioration of the fit quality.

To analyze the weak coherent oscillations in the AF phase, the three-exponential-fit residuals were fit once more by a sum of two damped cosine functions, $\sum A_i \exp(-\gamma_i t) \cos(\omega_i t + \delta_i)$, as shown in Fig. 6. Two oscillatory components with field independent frequencies and damping are observed in the AF phase, the stronger at ≈ 1.2 THz and the weaker at ≈ 1.4 THz [see Figs. 7(a) and 7(b)]. The weaker one is barely resolved from the noise; however, the damped cosine fit reliably locks to the frequency.

The above differences in the fit function components between the F phase and the other phases, however, do not necessarily imply that the fundamental physical origin of the nonoscillatory components differs in different phases. The dynamics of the degree associated with the oscillator in the F phase might become overdamped/exponential in the other phases. In such case one or more exponential

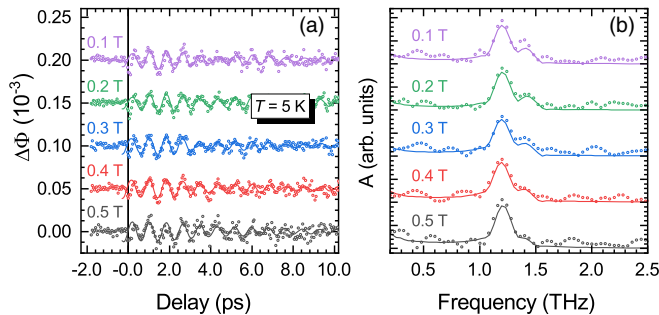


FIG. 5. Double damped cosine fit to the oscillations in the AF phase (a) and the corresponding Fourier transforms (b). The solid lines are fits and the traces are vertically shifted for clarity.

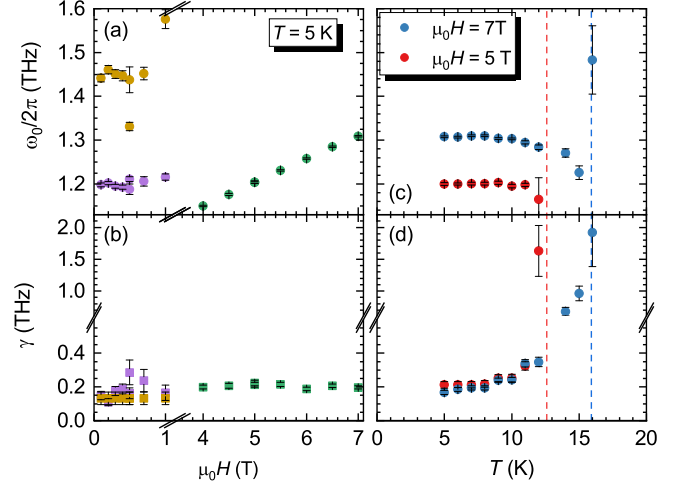


FIG. 7. Frequency and damping of the coherent oscillations in the AF and F phases as a function of H (a), (b) and in the F phase as a function of T (c), (d). The dashed lines represent the F phase boundaries from Chattopadhyay *et al.* [13].

components would replace the oscillatory ones. However, if their relaxation times would not significantly differ from τ_1 and τ_2 , their presence would result only in an apparent renormalization of the parameters of the three-exponential fit. Due to such possibility we therefore treat at this stage the nonoscillatory amplitudes as a metric of the signal, where in the F phase $A_{e1} + A_{O1}$, A_{O2} , and A_{O3} correspond to A_{e1} , A_{e2} , and A_{e3} in the other phases, respectively.

The field and temperature dependence of the frequencies and dampings obtained from the fits are shown in Fig. 7. In the F phase the frequency shows a linear dependence on H and is virtually T independent at $\mu_0 H = 5$ T while it shows $\approx 8\%$ softening above $T \approx 8$ K at $\mu_0 H = 7$ T. The damping, on the other hand, increases with increasing T and strongly diverges at the phase boundary to the FP₄ phase where the frequency also shows a strong anomaly. Since the fitting becomes rather unstable at these particular points the frequency anomaly is probably a fitting artifact.

The field dependence of other relevant fit parameters for the $T = 5$ K magnetic-field scan is shown in Figs. 8(a) and 8(b). The fast rise time, τ_1 , is significantly smaller in the F state (≈ 0.4 ps) than in the AF and both AFF phases (≈ 0.8 ps). It is virtually field independent within each of the phases. The slower rise time, τ_2 , on the other hand, appears the largest (≈ 12 ps), but with large error bars, in the AFF₂ phase while it is similar (≈ 5 ps) in the AF, AFF₁, and F phases with differences that are comparable to the data points scatter.

The amplitudes of the fast-rise-time components, A_{O1} (A_{e1}), and the nanosecond, $A_{O\infty}$ ($A_{e\infty}$), components [see Fig. 8(b)] behave in a similar manner but with opposite signs. The magnitudes are similar in the AF, AFF₁, and AFF₂ phases, but clearly smaller in the F phase, where in the F phase the sum $A_{e1} + A_{O1}$ is considered. The slow-rise-time component amplitude, A_{O2} , is significantly smaller than the fast component amplitude A_{e1} ($+A_{O1}$) in all phases.

The sign change of the transient response and the amplitudes going from the AFP₂ to AF phase could be linked

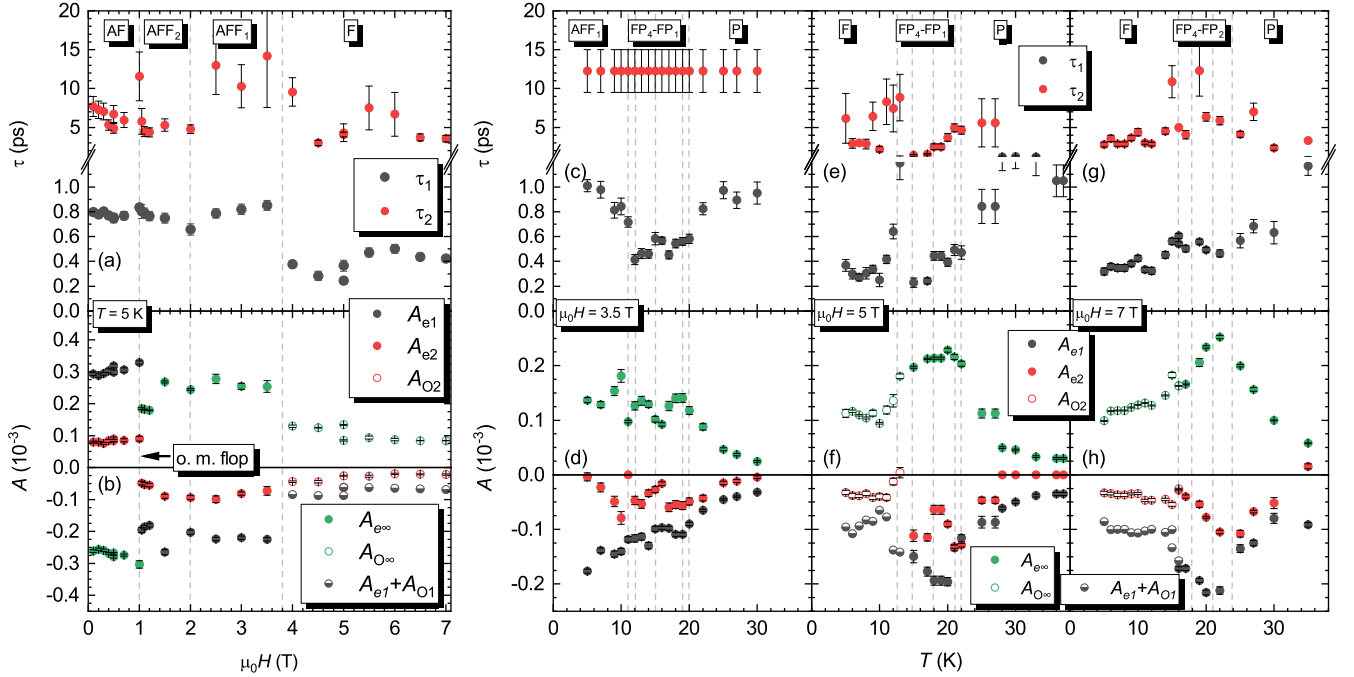


FIG. 8. Magnetic-field and temperature dependence of the selected DECO fit parameters. The open circles correspond to the oscillator while the full circles correspond to the exponential components. The half filled symbols correspond to the total amplitude (see text) of the fast exponential component in the F phase. The gray dashed lines represent the phase boundaries from Chattopadhyay *et al.* [13]. At the lowest field [$\mu_0 H = 3.5$ T, panels (c) and (d)] τ_2 was fit globally across all data sets to avoid the fit instabilities at some individual temperatures.

to the angular momentum flop transition of the spins (and concurrently the $[001]_T$ axis) from the $[100]$ easy axis in the F and AFF_n phases to the $[010]$ easy axis in the AF phase. The $[100]$ easy axis is oriented close to the magnetic-field direction and is thus energetically favorable in the phases with a finite magnetization while the $[010]$ easy axis is at much larger angle with respect to the field and energetically more favorable in the AF phase.

The temperature dependence of the relevant fit parameters at three different magnetic fields is shown in Figs. 8(c)–8(h). The fast rise time, τ_1 , in the AFF_1 phase shows a drop from $\tau_1 \approx 1$ to ≈ 0.7 ps with increasing T , but remains larger than in the F and FP_1 – FP_4 phases. In the F phase it is virtually T independent at $\tau_1 \approx 0.4$ ps. In the FP_1 – FP_4 phases it has a bit larger value, $\tau_1 \approx 0.5$ ps, than in the F phase. The two outlier points in the $\mu_0 H = 5$ T FP_3 phase, at $T = 12$ and 13 K [Fig. 8(e)], are most likely a consequence of a fit instability due to the vanishing coherent oscillations in this region. In the field-magnetized P phase it is scattered around ≈ 1 ps at the lowest two field magnitudes, while it continuously rises with increasing T at the highest field ($\mu_0 H = 7$ T) from the FP_2 phase value, $\tau_1 \approx 0.5$ ps, to an excess of 1 ps at $T = 36$ K.

The slower component rise time, τ_2 , shows quite large scatter, which is reflected also in the amplitude, A_{e2} , and no clear distinction between the different phases is observed. At the lowest field ($\mu_0 H = 3.5$ T) τ_2 was fit globally across all the relevant data sets to avoid fit instabilities at some individual temperatures.

Turning to the amplitudes, they are systematically lower in the F phase in comparison to the neighboring phases. With the exception of $A_{O\infty}$, which smoothly connects to the nanosecond exponential component amplitude, $A_{e\infty}$ with increasing

T , at $\mu_0 H = 7$ T [Fig. 8(h)], all component amplitudes show a steep increase at the F- FP_4 boundary. A similar, even sharper increase/discontinuity is observed also at the F- AFF_1 boundary around $\mu_0 H = 4$ T during the field scan at $T = 5$ K [see Fig. 8(b)].

IV. DISCUSSION

A. Coherent oscillations

To understand the origin of the coherent oscillations we compare the frequencies obtained using the transient optical spectroscopy to previous results obtained by means of different techniques. Inelastic neutron scattering (INS) measurements performed in the F phase at 4.2 K and 4.2 T show one peak at 4.2 meV (1.01 THz) at the Γ point. At these conditions CeSb is in the fully polarized F state with nearly complete saturation of the magnetic moment. On the basis of the INS results Halg and Furrer [3] proposed that CeSb can be considered as a two-level system in the F phase, because the molecular field dominates over the crystal field and the Ce^{3+} ion $4f$ levels in the ordered state are almost pure Zeeman levels. Their hypothesis was that the ground state is almost pure $|5/2\rangle$ and at low T the only possible magnetic excitation is a magnonlike transverse excitation from $|5/2\rangle$ to $|3/2\rangle$ state. At similar conditions, we optically observe a single magnetic mode, but at the frequency of 1.14 THz (4.7 meV), which is significantly (13%) larger (see Fig. 9).

There are two different reports on excitations in the AF state of CeSb. The INS measurements done by Halg and Furrer [3] revealed an excitation with energy of around 4.2 meV (1.01 THz) at the Γ point (see Fig. 9) that we have not observed optically. On the other hand, the Raman scattering

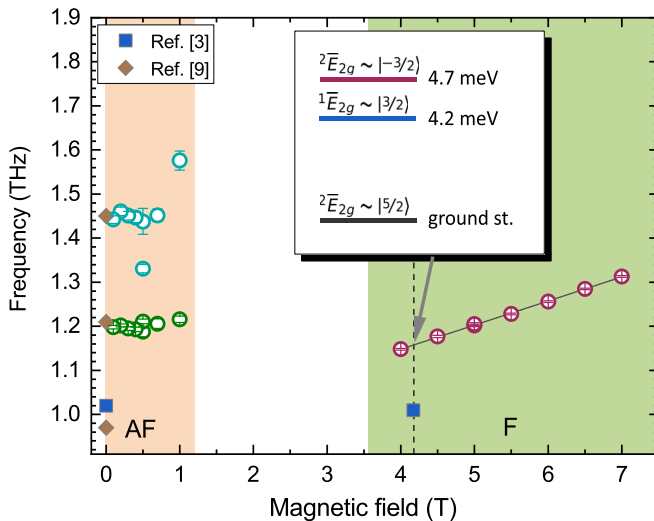


FIG. 9. Field dependence of the polarization rotation oscillations frequency (open symbols) compared to the literature data (full symbols). The frequencies of oscillations obtained in the antiferromagnetic state are very close to those obtained in [9]. From the fit of the frequency field dependence [Eq. (2)] in the ferromagnetic state (the solid line) we obtain the gyromagnetic ratio and anisotropy field, using the uniaxial ferromagnetic crystal model [15]. The schematics of the lowest Ce^{3+} $4f$ -derived Γ -point states in the F phase is shown in the inset.

measurements reported by Arai *et al.* [9] show additional excitations with energies of 5 meV (1.21 THz) and 6 meV (1.45 THz). Both energies coincide with our results. The 6-meV excitation was observed also in their INS spectra.

Looking from the point of the Ce^{3+} localized $4f$ crystal-field level excitations, the ground state in the magnetically ordered states must be close to the $|5/2\rangle$ state due to the almost saturated experimental magnetic moment and originates from the Γ_8 quartet [16,17]. The lowest energy excited state, which is observed by inelastic neutron scattering at ≈ 4.2 meV in AF and F phases [3], was proposed [17] to originate from the Γ_7 doublet. Totally one expects four more $4f$ excited states per Ce^{3+} ion.

For the corresponding collective states at the Brillouin zone (BZ) Γ point the single ion symmetries and splittings should apply in the P and F phases, while in the AF phase the number of Ce^{3+} ions in the primitive cell is increased to 4 resulting in 24 states totally. The local molecular field should split the single ion states, however some degeneracy persists (see Appendix D) due to the symmetry equivalence of the crystallographic sites within the AF tetragonal primitive cell.

In the present experiment we observe two coherent excitations in the AF phase that coincide with the Raman modes reported by Arai *et al.* [9] and should therefore have the same origin. Arai *et al.* assigned them to the magnetic excitonic transitions between Γ_8 -derived split states, possibly of vibronic character. The present paper indicates that the frequencies show virtually no magnetic-field dependence; however, this does not rule out the possible magnetic excitonic origin. Due to the angular momentum flop into the [010] easy-axis direction in the AF phase the sublattice magnetizations

become nearly perpendicular to the external magnetic field so the field dependence should be rather weak.

On the other hand, the BZ backfolding can result also in low frequency optical phonon modes. The phonon dispersions in ReSb [9,18] display a TA phonon branch dispersing up to ≈ 1.5 THz along the $\langle 00u \rangle$ direction. In the AF phase the cubic BZ points $(00u)$, where $u = 1$ and $\pm 1/2$, backfold to the Γ point, possibly producing optical phonons in the 1–1.5-THz frequency range. This should in principle be weak for magnetic ordering; however, in CeSb the magnetic ordering is accompanied with periodic lattice distortion in the AFP_n phases [6,19]. Moreover, a nondispersive optical phonon has been reported at 1.7 THz along the $\langle 0uu \rangle$ direction that appears below T_N in the AF phase [20]. The origin of the optically observed AF phase modes therefore remains unclear.

Due to the small signal to noise ratio and because the impulsive stimulated Raman scattering (ISRS) coherent-oscillations phase (see Fig. 6) can be arbitrary in absorbing materials [21], it is not possible to distinguish (by means of the fitting) whether the excitation of these modes in our experiment is via the ISRS or a displacive mechanism. The optical Raman transitions between any of the identical parity electronic states are allowed [22] in the nonmagnetic tetragonal D_{4h} symmetry already. ISRS excitation is therefore symmetry allowed for excitonic transitions in the ordered phases, which are weakly tetragonal. The absence of any pump polarization dependence indicates, however, that the coupling is not a tensor, suggesting that a displacive mechanism is more likely.

The displacive excitation can be more symmetry constrained. In bulk gapless materials the effective displacement is usually a scalar quantity, since any information about the initial photon polarization and wave vector is lost after the initial electron/hole pair is inelastically scattered on a femtosecond timescale. In such case the displacive excitation can be viewed as a fast Hamiltonian parameter quench. If such a quench is nonadiabatic the state of the system is no longer the ground state, but a linear combination of the eigenstates of the perturbed Hamiltonian, which exhibit time evolution. When the parameter quench preserves the Hamiltonian symmetry the linear combination of the perturbed eigenstates must transform identically to the original ground state, implying that the ground and displacive excited state must belong to an identical symmetry-group representation.

In the AF phase, the Ce^{3+} - $4f$ -levels derived states at the Γ point include (among others) four \bar{E}_{2g} symmetry states (see Table I). Assuming that one corresponds to the ground state there are three electronic excited states accessible by the displacive excitation.

Turning to the F phase, the frequency of the single coherent oscillation virtually linearly depends on the external magnetic field in a manner that would be expected for the ferromagnetic resonance (FMR) in the field parallel to an easy axis [23]. However, due to the finite optical penetration depth the oscillations can be excited only in a ≈ 50 -nm-thick surface layer² so the demagnetization FMR frequency shift needs to

²The optical penetration depth at the 3.1-eV pump photon energy is $\lambda_{\text{opt}} \approx 50$ nm and at the 1.55-eV probe photon energy ≈ 100 nm as estimated from the optical data in [24].

be taken into account when comparing to the INS results. With the external magnetic field parallel to the surface and nearly parallel to the [100] easy axis direction the Kittel FMR formula for a thin slab with an in-plane uniaxial anisotropy can be assumed:

$$\omega = \gamma_M \mu_0 \sqrt{(H + H_A)(H + H_A + M_0)}, \quad (2)$$

where H_A and M_0 correspond to the effective anisotropy field and the F phase magnetization, respectively, while $\gamma_M = g\mu_B/\hbar$ is the gyromagnetic ratio. Taking an almost saturated Ce^{3+} magnetic moment of, $\mu_{\text{Ce}^{3+}} \approx 2\mu_B$ [3], we get $\mu_0 M_0 \approx 0.4$ T, and obtain $g = 3.9$ and $\mu_0 H_A = 16.6$ T from the fit to the data shown in Fig. 9.

The large magnitude of the obtained g factor clearly indicates that the crystal-field effects are not significantly suppressed in the F phase, contrary to the earlier [3] suggestion, since $g \approx 0.9$ would be expected for pure Ce^{3+} Zeeman level splitting. Further, the magnitude of M_0 is *too small*³ to explain the 13% difference between the neutron and optical FMR frequencies by the shape anisotropy as it can account only for $\sim M_0/2H = 1.6\%$ demagnetization FMR frequency shift. The excited layer is also relatively thick in comparison to the atomic scale so any significant addition surface anisotropy can also be ruled out as the origin of the frequency difference.

Different sample strain in different experiments can also influence H_A and lead to different FMR/AFMR frequencies since the magnetic diagram of CeSb is quite sensitive to the external pressure [13,25]. In our experiment a millimeter size sample was glued by GE varnish on a copper holder and the surface far from the holder was used so the extrinsic strain due to the holder/sample thermal expansion mismatch is negligible. The only possible source of a significant strain could therefore be built-in strain related to the sample quality and growth conditions. However, the F-AFF₁ phase transition, which is pressure sensitive [25], is observed in our sample at the magnetic field value of $\mu_0 H = 3.65$ T [see Fig. 2(d)], giving no indication that built-in strain would be present.

The observed coherent oscillation therefore *cannot correspond* to the lowest-energy spin-wave-like branch observed by means of the INS [3] and is assigned to a magnetic excitonic excitation of another Ce^{3+} 4*f*-derived collective level. The group-theoretical symmetry analysis suggests (see Table II) that the ground state corresponds to the Γ -point ${}^2\bar{E}_{2g}$ (Γ_8^+) [10] symmetry and can be excited in a displacive manner (without any external symmetry-breaking field) only to the second ${}^2\bar{E}_{2g}$ (Γ_7^+) symmetry level. Considering the probe process one should analyze the Raman tensor for the transitions between these levels, which is of the A_g symmetry,⁴ consistent with the observed probe-polarization angular dependence (see Appendix C, Cracknell [26], and Fig. 12).

³It can account only for $\sim M_0/2H_0 = 1.6\%$ demagnetization FMR frequency shift.

⁴When inspecting Table I one should take into account that the matrix element [22] contains the conjugated final state wave function that can transform differently in the case of double groups. To obtain the Raman-transition tensor symmetry between two levels with ${}^2\bar{E}_{2g}$ symmetry one has to consider the direct product of ${}^2\bar{E}_{2g}^* \otimes {}^2\bar{E}_{2g} = {}^1\bar{E}_{2g} \otimes {}^2\bar{E}_{2g}$.

The ${}^2\bar{E}_{2g}$ levels are derived from the linear combinations of the $|^{-3/2}\rangle$ and $|5/2\rangle$ $\text{Ce}^{3+} {}^2F_{5/2}$ ionic states, which are mixed in the cubic crystal field already. Since the ground state has almost pure $|5/2\rangle$ character [3] the observed coherent-oscillation excitation should have dominating $|^{-3/2}\rangle$ character. The transition Δj_z is therefore ≈ 4 resulting in the $g_{\Delta j_z=1} \approx 1$, which is close to the ionic [27] $g_I = 6/7$. Considering the energy of the magnonlike $|3/2\rangle$ -character excitation [3] (see inset to Fig. 9) the level spacings therefore do not appear Zeeman-like so the crystal-field and quadrupolar bilinear interactions are relatively strong also in the magnetically ordered phases.

The independence of the pump polarization and the good quality of the DECP fits indicate that the excitation mechanism is displacive. On the microscopic level this could be clearly linked to the mixing of the $|^{-3/2}\rangle$ and $|5/2\rangle$ derived ${}^2\bar{E}_{2g}$ electronic states. The mixing should depend on the quasiparticle distribution function in the *p-f* hybridized conduction bands, which is, upon the photoexcitation, changed on a sub-picosecond scale. This corresponds to a nonadiabatic effective Hamiltonian quench, which leads to a change of the $|^{-3/2}\rangle$ - and $|5/2\rangle$ -derived wave functions mixing. As a result, a *quantum superposition state* of the $|^{-3/2}\rangle$ - and $|5/2\rangle$ -dominated ${}^2\bar{E}_{2g}$ wave functions, with a well-defined quantum phase, is created. The observed coherent oscillation therefore corresponds to the *real-time quantum evolution* and dephasing of the superposition state.

On the macroscopic level, the observable couples to the quadrupolar degrees of freedom according to the probe polarization angular dependence of the signal (see also Appendix C). The oscillation therefore could be associated with a direct coherent collective excitation of a (secondary) quadrupolar order parameter that is adjoined [28] to the dipolar order parameter in the unfilled 4*f* shell systems. Based on the symmetry (Appendix C) such excitation couples to the longitudinal modulation of the dipolar (magnetization) order parameter.

The absence of the coherent oscillations due to the lowest energy transition to the collective transverse spin-wave-like state with the ${}^1\bar{E}_{2g}$ ($|3/2\rangle$) character observed by INS [3] is somewhat surprising. The displacive excitation is symmetry allowed due to the external symmetry-breaking magnetic field,⁵ which is at a finite angle with respect to the [100] axis. However, due to the tetragonal symmetry the transverse magnetization components couple quadratically to the reflectivity in the lowest order (see Appendix C) and are likely below the detection limit.

Reasons for the absence of any coherent modes in the FP_{*n*} and AFF_{*n*} magnetic phases are unclear. There is no fundamental account prohibiting their coupling to the optical probe and the nonoscillating components are qualitatively similar in all phases, suggesting that the same degrees of freedom are involved. A possible reason could be a larger dephasing. Different intrinsic dephasing (on the quantum level) due to different electron scattering in different phases [10]

⁵In Ni, for example, spin waves can be displacively excited [29] when the external magnetic field is applied at some angle to the anisotropy field.

would be plausible, since it is clearly different in different phases [30,31]. On the other hand, stronger disorder, which contributes to the dephasing, could also be expected in the intermediate phases due to their larger magnetic unit cells and similar free energies. As a result, long magnetostructural coherence lengths are unlikely, especially in the presence of the pulsed laser perturbation.

B. Nonoscillatory response

Turning to the nonoscillatory relaxation components we observe a qualitatively similar response in all phases. The probe polarization dependence and the presence of the components in the external-field-magnetized P phase suggest that it could be linked (on a phenomenological level) to the longitudinal transient sublattice magnetization which is strongly coupled to the electronic structure due to the p - f mixing [30,31].

The dynamics is driven by the nonequilibrium carrier redistribution and their excess energy transfer to the lattice. Due to the absence of the gap it is not surprising that the dominant relaxation is happening on a (sub)picosecond timescale. The difference of this timescale in different phases can be attributed to their electronic structures [31]. The similar $\tau_1 \approx 1$ ps in the AF, AFF₁, and AFF₂ suggests that their electronic structure is similar, while significantly shorter $\tau_1 \approx 0.5$ ps in the FP₁₋₄ phases indicates that their electronic structure is more similar to the F phase. The minor and slower signal-rise component timescale could also be of a related origin involving different parts of the Fermi surface. However, in order to obtain more detailed insight, kinetics models of the relaxation would need to be solved, which is beyond the scope of the present paper.

V. SUMMARY AND CONCLUSIONS

We performed time-resolved measurements of the magneto-optic response in CeSb with systematic variation of the temperature and magnetic field to obtain the transient magneto-optic response in different magnetically ordered phases.

In the AF and F phases we observe damped coherent oscillations of the magneto-optic response. In the fully polarized F phase, a single coherent oscillation is observed with the spectroscopic g factor, $g = 3.94$. The observed frequency differs by 13% from the Γ -point inelastic-neutron-scattering observed magnetic excitation [3]. The oscillation is attributed to the *real-time coherent quantum evolution* of the displacively induced *quantum superposition* of the magnetic excitonic $\text{Ce}^{3+} - 4f$ -derived collective states. The finding opens the way for the possibility to control such excitonic collective states on the quantum level.

The coherent oscillation frequency and the magnitude of the g factor together with the detailed group-theoretical symmetry analysis put the $|^{-3/2}$ -character ${}^2\bar{E}_{2g}$ level in the vicinity of the $|^{3/2}$ -character ${}^1\bar{E}_{2g}$ level. This indicates that the level spacing is, contrary to the literature [3], not Zeeman-like and the crystal-field and quadrupolar bilinear interactions are relatively strong also in the magnetically ordered phases.

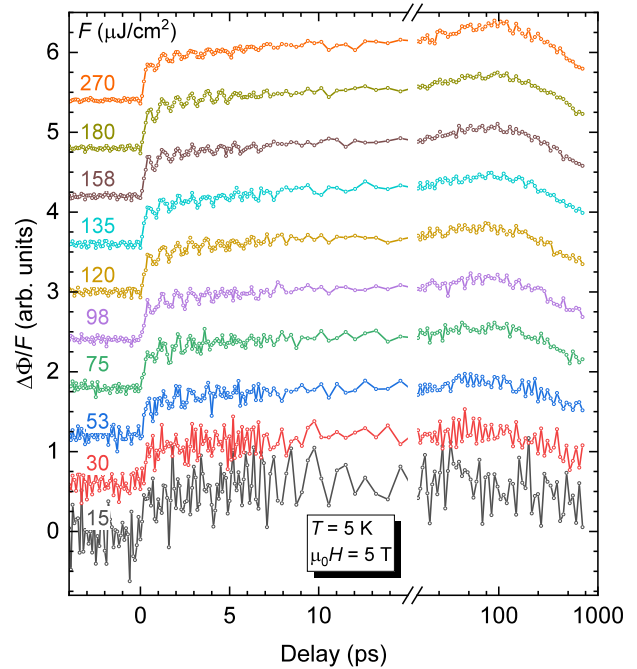


FIG. 10. Fluence dependence of the normalized transient polarization rotation at $T = 5$ K and $\mu_0 H = 5$ T. Note the logarithmic scale after the break.

In the AF phase two weaker coherent oscillations with *magnetic-field-independent* frequencies of 1.20 and 1.45 THz are observed. The frequencies correspond to the modes recently observed also by means of Raman scattering [14]. While it is likely that the modes have the magnetic excitonic origin, as in the F phase, the lattice origin cannot be entirely ruled out.

The nonoscillatory part of the transients shows faster subpicosecond dynamics in the F and FP₁₋₄ phases in comparison to the AF, AFF₁, and AFF₂ phases. This suggests that the electronic structures, which affect the kinetics of the hot electron energy relaxation, in the F and FP_n differ from the electronic structures in the AF, AFF₁, and AFF₂ phases.

ACKNOWLEDGMENTS

The authors acknowledge the financial support of Slovenian Research and Innovation Agency (research core funding Grant No. P1-0040 and young researcher funding Grant No. 50504). We would also like to thank V. V. Kabanov and A. Shumilin for fruitful discussions.

APPENDIX A: PUMP FLUENCE DEPENDENCE OF OPTICAL TRANSIENTS

In Fig. 10 we show the pump fluence dependence of $\Delta\Phi$. The fluence normalized scans are virtually F independent, indicating a linear scaling of the transients with increasing F .

APPENDIX B: DISPLACIVE EXCITATION OF COHERENT OSCILLATIONS

Following the standard derivation [14] for the displacive driven oscillator we assume a single harmonic oscillator driven by a displacement composed from three pulse-driven exponential components (1) and obtain

$$\Delta\Phi(t) = \sum \left\{ (A_{ej} + A_{Oj}) \int_0^\infty G(t-u) \exp^{-u/\tau_j} du - A_{Oj} \int_0^\infty G(t-u) \exp^{-\gamma u} \times [\cos(\Omega u) - \beta_j \sin(\Omega u)] du \right\}, \quad (\text{B1})$$

where

$$\beta_j = (1/\tau_j - \gamma)/\Omega \quad (\text{B2})$$

$$G = \begin{bmatrix} c_{11}M_x^2 + c_{21}(M_y^2 + M_z^2) & c_{55}M_xM_y & c_{55}M_xM_z \\ c_{55}M_xM_y & c_{11}M_y^2 + c_{21}(M_x^2 + M_z^2) & c_{55}M_yM_z \\ c_{55}M_xM_z & c_{55}M_yM_z & c_{11}M_z^2 + c_{21}(M_x^2 + M_y^2) \end{bmatrix}, \quad (\text{C1})$$

where c_{ij} correspond to the three independent coefficients and M_j corresponds to the magnetization components. Assuming the static magnetization, M_0 , along [100] the tensor can be linearized with respect to the transient magnetization, $(\Delta M_x, \Delta M_y, \Delta M_z)$:

$$G \approx \begin{bmatrix} c_{11}(M_0^2 + 2M_0\Delta M_x) & c_{55}M_0\Delta M_y & c_{55}M_0\Delta M_z \\ c_{55}M_0\Delta M_y & c_{21}(M_0^2 + 2M_0\Delta M_x) & 0 \\ c_{55}M_0\Delta M_z & 0 & c_{21}(M_0^2 + 2M_0\Delta M_x) \end{bmatrix}. \quad (\text{C2})$$

The off-diagonal components couple to the transverse transient magnetization while the diagonal components couple to the longitudinal one.

and

$$G(t) = \sqrt{\frac{2}{\pi}} \frac{1}{\tau_p} e^{-\frac{t}{\tau_p}}. \quad (\text{B3})$$

The amplitudes of the exponential displacement components with relaxation times, τ_j , are given by A_{Oj} , while Ω and γ correspond to the oscillator (renormalized) frequency and damping, respectively. τ_p corresponds to the effective pump-probe pulse cross-correlation width. A_{ej} allow for the possibility that any of the exponential displacement components contributes also directly to the optical response.

APPENDIX C: POLARIZATION ROTATION DUE TO COTTON-MOUTON EFFECT IN THE CUBIC SYMMETRY

The second-order magneto-optical tensor describing the magnetic linear dichroism and birefringence in $Fm\bar{3}m$ symmetry is given by [32]

Constraining the light propagation along the [001] direction one obtains

$$\begin{aligned} \Delta R/R &= [a + b \cos(2\phi)]M_0\Delta M_x + o(\Delta M_x^2, \Delta M_y^2), \\ \Delta\Phi &= b \sin(2\phi)M_0\Delta M_x + o(\Delta M_x^2, \Delta M_y^2), \end{aligned} \quad (\text{C3})$$

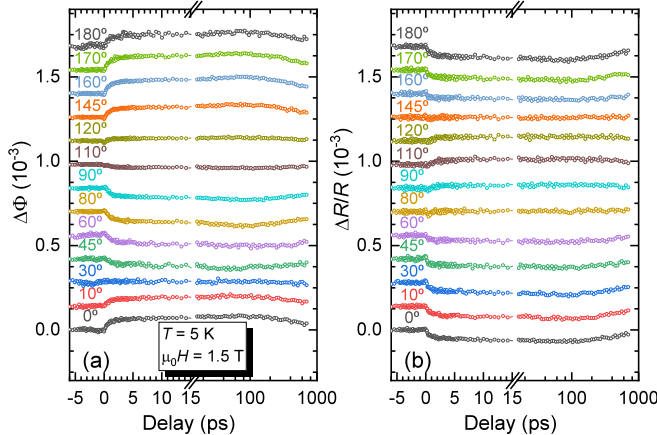


FIG. 11. Angular dependence of (a) polarization rotation and (b) reflectivity transients at $T = 5$ K and $\mu_0 H = 1.5$ T, in the AFF_2 phase. Note the logarithmic scale after the breaks.

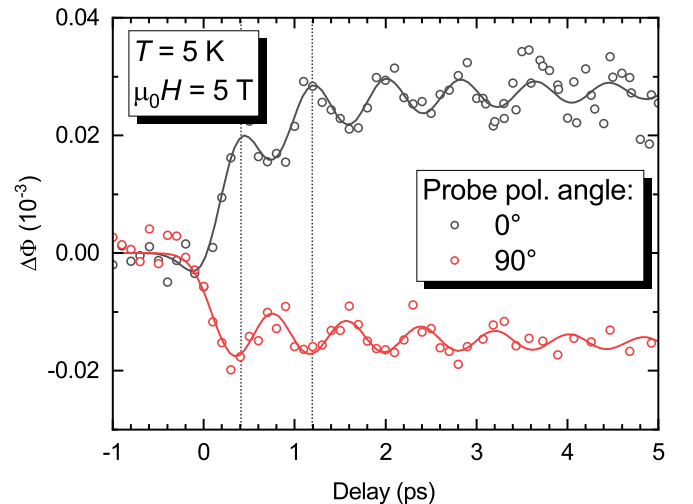


FIG. 12. Effect of the probe polarization on the polarization rotation in the F phase. The solid lines are the DECO (B1) fits.

TABLE I. Irreducible corepresentations of the Ce^{3+} ion $J = 5/2$ $4f$ (${}^2F_{5/2}$) multiplet derived states at the Brillouin zone Γ point and direct product decompositions of the relevant corepresentations.

Phase	P				F	AF		
Magnetic space group	$Fm\bar{3}m$				$I4/m\bar{m}'m'$	P_64/ncc		
Point group at Γ	$m\bar{3}m$				$4/m\bar{m}'m'$	$4/m\bar{m}m1'$		
Ce^{3+} site symmetry	$m\bar{3}m$ (4a)				$4/m\bar{m}'m'$ (2a)	$4m'm'$ (4c)		
Induced $J = 5/2$ multiplet	$\begin{cases} \bar{E}_{2g}(\Gamma_7^+) \\ \bar{F}_g(\Gamma_8^+) \end{cases}$				${}^1\bar{E}_{2g} \oplus {}^2\bar{E}_{2g}$	$2\bar{E}_{2g} \oplus 2\bar{E}_{2u}$		
irreducible band corepresentations	$\begin{cases} \bar{E}_{2g}(\Gamma_7^+) \\ \bar{F}_g(\Gamma_8^+) \end{cases}$				${}^1\bar{E}_{1g} \oplus {}^2\bar{E}_{1g} \oplus {}^1\bar{E}_{2g} \oplus {}^2\bar{E}_{2g}$	$2\bar{E}_{1g} \oplus 2\bar{E}_{2g} \oplus 2\bar{E}_{1u} \oplus 2\bar{E}_{2u}$		
$4/m\bar{m}'m'$ (F)	${}^1\bar{E}_{1g}$	${}^2\bar{E}_{1g}$	${}^1\bar{E}_{2g}$	${}^2\bar{E}_{2g}$				
${}^1\bar{E}_{1g}$	2E_g	A_g	1E_g	B_g	$4/m\bar{m}m1'$ (AF)	\bar{E}_{1g}	\bar{E}_{2g}	
${}^2\bar{E}_{1g}$	A_g	1E_g	B_g	2E_g	\bar{E}_{1g}	$A_{1g} + A_{2g} + E_g$	$B_{1g} + B_{2g} + E_g$	
${}^1\bar{E}_{2g}$	1E_g	B_g	2E_g	A_g	\bar{E}_{2g}	$B_{1g} + B_{2g} + E_g$	$A_{1g} + A_{2g} + E_g$	
${}^2\bar{E}_{2g}$	B_g	2E_g	A_g	E_{1g}				

where ϕ corresponds to the probe polarization angle with respect to the [100] direction. a and b are rational polynomial functions of the real, n , and imaginary part, k , of the probe refraction index as well as the magneto-optical tensor factors c_{11} and c_{21} . Unless $|c_{55}\Delta M_y| > |(c_{21} - c_{11})M_0|$, the dependence on ΔM_y is quadratic. Both the transient reflectivity and polarization rotation couple to the longitudinal transient magnetization, ΔM_x , only. The behavior is similar also in the tetragonal case when both the tetragonal axis and M_0 are oriented along the pseudocubic [100] or [010] directions.

The transverse transient magnetization along the light propagation direction, ΔM_z , can be detected through the polar magneto-optic Kerr effect at any probe polarization if the coupling constant is large enough. The coupling is linear and the probe polarization is independent only when $|\alpha\Delta M_z| > |(c_{21} - c_{11})M_0|$, with αM_z corresponding to the component of the magneto-optical gyration [33] vector.

TABLE II. Transformation properties of the $J = 5/2$ multiplet base functions in the F-state magnetic point group $4/m\bar{m}'m'$.

Corep.	Base func.
${}^1\bar{E}_{1g}$	$ -1/2\rangle$
${}^2\bar{E}_{1g}$	$ 1/2\rangle$
${}^1\bar{E}_{2g}$	$ -5/2\rangle, 3/2\rangle$
${}^2\bar{E}_{2g}$	$ 5/2\rangle, -3/2\rangle$

In our case (see Figs. 4, 11, and 12) the experimental extrema of the transient reflectivity amplitude are for probe polarizations along [100] and [010] crystal directions while the transient polarization rotation is shifted by $\approx 50^\circ$ with respect to the transient reflectivity. Both signals are therefore dominated by the modulation of the diagonal dielectric tensor components that couple (on the macroscopic level) to the the longitudinal transient magnetization as well as the orthorhombic anisotropy of the electronic system.

APPENDIX D: SYMMETRY CONSIDERATIONS

In the paramagnetic phase ($Fm\bar{3}m$) the Ce^{3+} ion $4f$ $J = 5/2$ multiplet derived states correspond to two-dimensional \bar{E}_{2g} (Γ_7^+) and four-dimensional \bar{F}_g (Γ_8^+) representations of the Γ point group ($m\bar{3}m$). Assuming the highest possible symmetry magnetic groups compatible with the experimental tetragonal symmetry [34] we obtain [35] $I4/m\bar{m}'m'$ (no. 139.537) and P_64/ncc (no. 130.432) magnetic groups for the F and AF state, respectively. In the F phase⁶ the Γ -point degeneracy is completely removed while in the AF phase the states remain doubly degenerate (see Table I) [36,37]. Moreover due to the Brillouin zone folding [4] an additional 18 backfolded $4f$ -derived bands appear at the Γ point in the AF phase.

Looking at the direct products of the involved corepresentations [37] (see Table I), all transitions are Raman allowed.

⁶In an external magnetic field along a fourfold axis in the P phase as well.

- [1] J. Rossat-Mignod, P. Burlet, J. Villain, H. Bartholin, W. Tcheng-Si, D. Florence, and O. Vogt, *Phys. Rev. B* **16**, 440 (1977).
- [2] J. Rossat-Mignod, J. Effantin, P. Burlet, T. Chattopadhyay, L. Regnault, H. Bartholin, C. Vettier, O. Vogt, D. Ravot, and J. Achart, *J. Magn. Magn. Mater.* **52**, 111 (1985).
- [3] B. Halg and A. Furrer, *Phys. Rev. B* **34**, 6258 (1986).
- [4] S. Jang, R. Kealhofer, C. John, S. Doyle, J.-S. Hong, J. H. Shim, Q. Si, O. Erten, J. D. Denlinger, and J. G. Analytis, *Sci. Adv.* **5**, eaaf7158 (2019).
- [5] T. Kasuya, Y. Kwon, T. Suzuki, K. Nakanishi, F. Ishiyama, and K. Takegahara, *J. Magn. Magn. Mater.* **90-91**, 389 (1990).
- [6] D. F. McMorrow, J.-G. Lussier, B. Lebech, S. A. Sørensen, M. J. Christensen, and O. Vogt, *J. Phys.: Condens. Matter* **9**, 1133 (1997).
- [7] J. Rossat-Mignod, J. Effantin, C. Vettier, and O. Vogt, *Physica B+C* **130**, 555 (1985).
- [8] K. Kuroda, Y. Arai, N. Rezaei, S. Kunisada, S. Sakuragi, M. Alaei, Y. Kinoshita, C. Bareille, R. Noguchi, M. Nakayama, S.

- Akebi, M. Sakano, K. Kawaguchi, M. Arita, S. Ideta, K. Tanaka, H. Kitazawa, K. Okazaki, M. Tokunaga, Y. Haga *et al.*, *Nat. Commun.* **11**, 2888 (2020).
- [9] Y. Arai, K. Kuroda, T. Nomoto, Z. H. Tin, S. Sakuragi, C. Bareille, S. Akebi, K. Kurokawa, Y. Kinoshita, W.-L. Zhang, S. Shin, M. Tokunaga, H. Kitazawa, Y. Haga, H. S. Suzuki, S. Miyasaka, S. Tajima, K. Iwasa, R. Arita, and T. Kondo, *Nat. Mater.* **21**, 410 (2022).
- [10] L. Ye, T. Suzuki, C. R. Wicker, and J. G. Checkelsky, *Phys. Rev. B* **97**, 081108(R) (2018).
- [11] P. C. Canfield, *Rep. Prog. Phys.* **83**, 016501 (2020).
- [12] T. Wiener and P. Canfield, *J. Alloys Compd.* **303-304**, 505 (2000).
- [13] T. Chattopadhyay, P. Burtel, J. Rossat-Mignod, H. Bartholin, C. Vettier, and O. Vogt, *Phys. Rev. B* **49**, 15096 (1994).
- [14] H. J. Zeiger, J. Vidal, T. K. Cheng, E. P. Ippen, G. Dresselhaus, and M. S. Dresselhaus, *Phys. Rev. B* **45**, 768 (1992).
- [15] E. Turov, *Physical Properties of Magnetically Ordered Crystals* (Academic, New York, 1965).
- [16] J. Boucherle, A. Delapalme, C. Howard, J. Rossat-Mignod, and O. Vogt, *Physica B+C* **102**, 253 (1980).
- [17] H. Takahashi and T. Kasuya, *J. Phys. C* **18**, 2731 (1985).
- [18] B. Rakshit, V. Srivastava, S. Sanyal, N. Dilawar, D. Varandani, and A. Bandyopadhyay, *Optoelectron. Adv. Mat.* **2**, 37 (2008).
- [19] K. Iwasa, Y. Arakaki, M. Kohgi, and T. Suzuki, *J. Phys. Soc. Jpn.* **68**, 2498 (1999).
- [20] K. Iwasa, A. Hannan, M. Kohgi, M. Braden, J.-M. Mignot, H. Kitazawa, and T. Suzuki, *Appl. Phys. A* **74**, s1779 (2002).
- [21] T. E. Stevens, J. Kuhl, and R. Merlin, *Phys. Rev. B* **65**, 144304 (2002).
- [22] A. Kiel and S. Porto, *J. Mol. Spectrosc.* **32**, 458 (1969).
- [23] C. Kittel, *J. Phys. Radium* **12**, 291 (1951).
- [24] Y. Kwon, M. Takeshige, T. Suzuki, and T. Kasuya, *Phys. B: Condens. Matter* **163**, 328 (1990).
- [25] H. Bartholin, D. Florence, and O. Vogt, *J. Phys. Chem. Solids* **39**, 89 (1978).
- [26] A. P. Cracknell, *J. Phys. C* **2**, 500 (1969).
- [27] P. Fulde and M. Loewenhaupt, *Adv. Phys.* **34**, 589 (1985).
- [28] P. Morin and D. Schmitt, *Handbook of Ferromagnetic Materials* (Elsevier, Amsterdam, 1990), Vol. 5, pp. 1–132.
- [29] M. van Kampen, C. Jozsa, J. T. Kohlhepp, P. LeClair, L. Lagae, W. J. M. de Jonge, and B. Koopmans, *Phys. Rev. Lett.* **88**, 227201 (2002).
- [30] H. Aoki, G. Crabtree, W. Joss, and F. Hulliger, *J. Magn. Magn. Mater.* **52**, 389 (1985).
- [31] Y. Kaneta, S. Iwata, T. Kasuya, and O. Sakai, *J. Phys. Soc. Jpn.* **69**, 2559 (2000).
- [32] S. V. Gallego, J. Etxebarria, L. Elcoro, E. S. Tasci, and J. M. Perez-Mato, *Acta Crystallogr. Sect. A* **75**, 438 (2019).
- [33] A. K. Zvezdin and V. A. Kotov, *Modern Magneto-optics and Magneto-optical Materials*, Studies in Condensed Matter Physics (Institute of Physics, University of Reading, Berkshire, 1997).
- [34] F. Hulliger, M. Landolt, H. R. Ott, and R. Schmelczer, *J. Low Temp. Phys.* **20**, 269 (1975).
- [35] J. M. Perez-Mato, S. V. Gallego, E. S. Tasci, L. Elcoro, G. de la Flor, and M. I. Aroyo, *Annu. Rev. Mater. Res.* **45**, 217 (2015).
- [36] L. Elcoro, Z. Song, and B. A. Bernevig, *Phys. Rev. B* **102**, 035110 (2020).
- [37] A. P. Cracknell, *Adv. Phys.* **17**, 367 (1968).